RSC Advances

ROYAL SOCIETY OF CHEMISTRY

www.rsc.org/advances

Advances

Communication

Role of propane sultone as additive to improve the performance of lithium-rich cathode material at high potential

Julie Pires[a], Laure Timperman[a], Aurore Castets[b], Jésus Santos Peña[a], Erwan Dumont[c], Stéphane Levasseur[d], Rémi Dedryvère[b], Cécile Tessier[c], Mérièm. Anouti[a] *

Abstract

This study presents the use of 1,3-propane sultone (PS) in the [EC/DMC + 1 mol L^{-1} $LiPF_6$] electrolyte as a protective additive for the Li-rich-NMC $x$$Li_2MnO_3$–$(1-x)LiMO_2$ (x>>1; M = Ni, Co, Mn) cathode/electrolyte interface during the cathode material activation and cycling at high potential (5 V vs. Li). The results showed that the presence of 1% PS (w/w) ensured complete and better electrode activation during the first cycle than EC/DMC + 1 mol L^{-1} $LiPF_6$. Thus, Li// Li-rich-NMC half-cell and Gr// Li-rich-NMC full-cell provided capacities as high as C = 330 during charge mAh g^{-1} and C = 275 mAh g^{-1} during discharge with a higher cut-off voltage of 5 V. Measurements by cyclic voltammetry demonstrated that activating at such a voltage enhanced the redox activity from Li_2MnO_3 activation. Simultaneously, to enhance "Li_2MnO_3", electroactivity decreased the nickel and cobalt contributions at their regular voltages. This feature was attributed to structural modifications occurring from the surface to the bulk of the material. Long-cycling tests of Li// Li-rich-NMC half-cells with PS provided a higher reversible capacity and superior capacity retention (245 mAh g^{-1} after 240 cycles) with good coulombic efficiency (99 ± 1%) and better high-discharge rate capability (above 180 mAh g^{-1} at 1 C regime) than those obtained by using conventional electrolytes without additive.

1. Introduction

Although layered Li-rich-NMC cathodes with the specific $x$$Li_2MnO_3$–$(1-x)LiMO_2$ (x>>1) dual structure may provide remarkable high-specific capacities compared to standard NMC[1, 2], their practical application is still limited due to unsolved issues [3-5]. For instance, transformation from a layered to spinel-layered intergrowth structure in the activation process during the initial charge leads to oxygen release during the first charge [6], lowering the oxidation state of transition metal ions at the end of the subsequent discharge. This redox process leads to continuous decay of the discharge plateau by various metal dissolutions and increases the oxidation states of the remaining transition metals at the surface regions of the Li-rich-NMC particles[7]. The consequences of these combined phenomena cause accelerated electrolyte decomposition and hence, severe decreased capacity during long-term cycling [8].

Various strategies have been developed to improve the electrochemical performance of these materials by controlling the particle size within the nanometer scale [9], morphology and composition of interior micro-/nanostructures or by controlling the structural homogeneity and affording a narrow particle-size distribution [10]. The major drawbacks of spinel-layered intergrowth formed after activation are its structural instability at high potential and manganese dissolution into the electrolyte subsequent to the electrode attack by hydrofluoric acid (HF) produced by the reaction of $LiPF_6$ and traces of H_2O in the electrolyte.

Notably, using electrolyte additives is a very efficient and economic means of obtaining the desired cell functionality. Adsorbed or solid species on the cathode surface could alleviate the undesirable exothermic reaction between the delithiated cathode and the electrolyte[11]. Various additives in the electrolyte are devoted to the formation of a stable SEI on the graphite anode or a protective film on selected cathodes. The best lithium-ion battery performance has been shown by the addition of additives such as vinylene carbonate (VC)[12], ethylene sulfite (ES) [13], 1,4-butane sultone (BS) [14], vinylethylene carbonate [15], and/or lithium bis(oxalate)borate (LiBOB)[16] to conventional electrolytes based on alkyl-carbonates. These additives are generally more easily electroactivated than the electrolyte, creating an effective layer during the first cycle and consequently protecting the electrode/electrolyte from decomposition. Although the beneficial effects of these additives on anodes are reasonably well understood, the effects on the Li-rich cathode have been reported rarely. Yang *et al*. examined the use of tris(hexafluoro-iso-propyl)phosphate (HFiP) as a cathode "SEI" former for a 5 V class

spinel LNMO cathode to improve the electrochemical performance of the Li[Li$_{0.2}$Mn$_{0.56}$Ni$_{0.16}$Co$_{0,08}$]O$_2$ cathode [17]. More recently, Choi *et al.* demonstrated the good effect of LiBOB as an oxidative additive to prevent decomposition of the electrolyte on the surface of the Li-rich cathode in half-cells and full-cells based on a graphite anode[18]. 1,3-Propane sultone (PS) is well known to suppress swelling of batteries at elevated temperature [19] by preventing the electrolyte reaction with oxygen produced by the cathode materials (such as Li$_x$CoO$_2$, Li$_x$Mn$_2$O$_4$, and Li$_x$NiO$_2$) at elevated temperature [20, 21]. In this study, we used PS as additive to improve the cycling ability of the Li-rich-NMC cathode with a high-limit potential up to 5 V.

2. Materials and methods

All compounds used in the electrolyte formulation were purchased from Sigma Aldrich with purity > 99.9% and were used without further purification. Ethylene carbonate (EC) and dimethyl carbonate (DMC) in a binary mixture 1:1 (w/w) with 1 mol L^{-1} LiPF$_6$ was selected as a baseline electrolyte. 1,3-propane sultone (PS) additive was added (1% in weight ratio) to this baseline electrolyte. Electrolyte preparation occurred in an argon-filled glove box with oxygen and water contents lower than 1 ppm.

Viscosities were measured using an Anton Parr digital vibrating tube densitometer (model 60/602, Anton Parr, France) and an Anton Parr rolling-ball viscometer (model Lovis 2000 M/ME, Anton Parr, France). A Crison (GLP 31) digital multifrequency conductimeter was used to measure the ionic conductivities. Temperature control from 25 °C to 80 °C was ensured by a JULABO F25 thermostated bath with an accuracy of ± 0.2 °C.

Electrochemical properties of the Li-rich-NMC cathode were evaluated with a VMP multichannel potentiostatic-galvanostatic system (Biologic Science Instrument, France) using Swagelok-type cells for the cyclic voltammetry (CV) and electrochemical impedance spectroscopy (EIS) measurements. Galvanostatic cycling was performed on coin-cells under different regimes: C/10, C/5 and C where C was the courant associated with the theoretical extraction/insertion of one mole of lithium per mole of active material in one hour. All systems were assembled in the glove box. A double microfiber separator drenched with the electrolyte was used for all tests. Highly pure lithium foil was used as the counter electrode and reference electrode. XPS measurements were carried out with a Kratos Axis Ultra spectrometer, using a focused monochromatized Al Kα radiation, directly connected through a transfer chamber to an argon dry box, in order to avoid moisture/air exposure of the samples. After electrochemical experiments the positive electrode was carefully separated from other battery components in the argon dry box, washed with DMC solvent to remove the electrolyte, and dried prior to being introduced into the XPS vacuum chamber. Further details can be found elsewhere[22].

3. Results and discussion

### 3.1 Characterization of electrolyte

Figure 1 shows the conductivity and viscosity of EC/DMC (w/w) + 1M LiPF$_6$ (red) and EC/DMC (w/w) + 1M LiPF$_6$ with 1% PS (which corresponded to 5% in molar fraction) as electrolytes from 10 to 80 °C.

From this figure, can be show that although the viscosity of the mixture with PS was unfavorable at any temperature, the conductivity of PS-based electrolyte is better In fact, the Walden product (σ.η) is more appropriate to compare ion mobility in different electrolytes. Table 1 presents the comparative values at 25 °C and 60 °C for both electrolytes.

Table 1. Comparison of conductivity, viscosity and Walden product (W = σ.η) for (EC/DMC; w/w) + 1 mol L^{-1} LiPF$_6$ with and without 1% PS

	EC/DMC (w/w) 1 M LiPF$_6$		EC/DMC (w/w) 1 M LiPF$_6$ + 1% PS	
T	25°C	60°C	25°C	60°C
σ (mS cm^{-1})	12.6	20.8	13.1	22.2
η (mPa s)	3.26	1.77	3.68	1.99
W (mS mPa cm^{-1} s)	41.07	36.81	48.21	43.78

The best transport properties observed with 1% of PS (referred to EC/DMC) shown by the Walden values can be explained by the compromise between fluidity in presence of PS and favorable solvation of the lithium cation by charge distribution in the electron-rich region in the PS ring (insert in **Figure 1**), which exceeded that of the EC/DMC binary mixture.
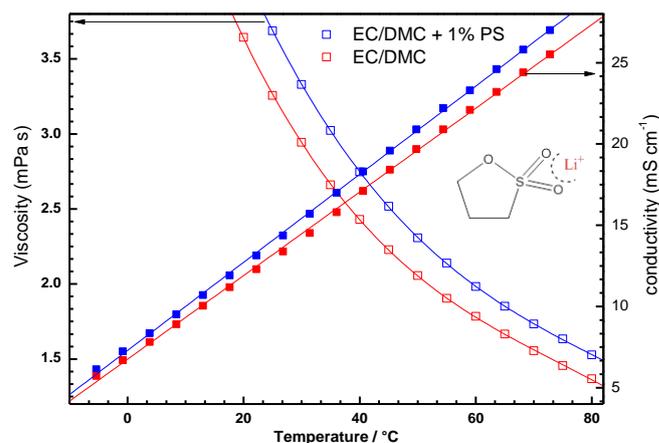
Figure 1. Evolution of the conductivity, σ, viscosity, η, according to temperature for (EC/DMC) + 1 mol L^{-1} LiPF$_6$ with (blue) and without (red) 1% PS.

3.2.1 Initial charge and discharge properties

To evaluate the redox process during the so-called activation step (high-voltage plateau during the first cycle) and its evolution during the following cycles, cyclic voltammetry (CV) analysis was conducted in Swagelok-type cells in the range potential from 2 V to 5 V versus Li$^+$/Li at 20 µV s^{-1}. Figure 2a (red dashed curve) shows the two main oxidation peaks: the first one located around 4.0V and the second one close to 4.6V during the initial charge. The peak at low potential was attributed to oxidation of nickel and cobalt from Ni^{2+} to Ni^{4+} and Co^{3+} to Co^{4+} [23]. At higher potential, the peak at 4.6 V is related to the so-called activation process responsible for the extra capacity of these materials.

During the subsequent discharge, the anodic curve contained three peaks located close to 4.4 V, 3.7 V and 3.1 V. The partial reversibility of the process responsible for the large charging capacity (oxidation peak at 4.6V) leads to the reduction peak at 4.4V in discharge. The peak at 3.7 V corresponds to the reversible reduction of Co^{4+} to Co^{3+} and Ni^{4+} to Ni^{2+}. The peak at 3.1 V corresponds to the reduction Mn^{4+} to Mn^{3+}. The last couple was activated upon cycling as the reduction peak at 3.1 V and its oxidation counter-part at 3.2V become more and more intense at each cycle. Conversely, the electroactivity of nickel and cobalt redox couples decreased upon cycling.

From the sixth cycle (Figure 2b), a drastic CV profile change occurred. Indeed, the reduction/oxidation peaks are shifted, which correspond to important kinetic limitations. Important structural

modifications of the material could be at the origin of these kinetic limitations, such as the formation of spinel phase due to the very high upper limit voltage (5V)[3].
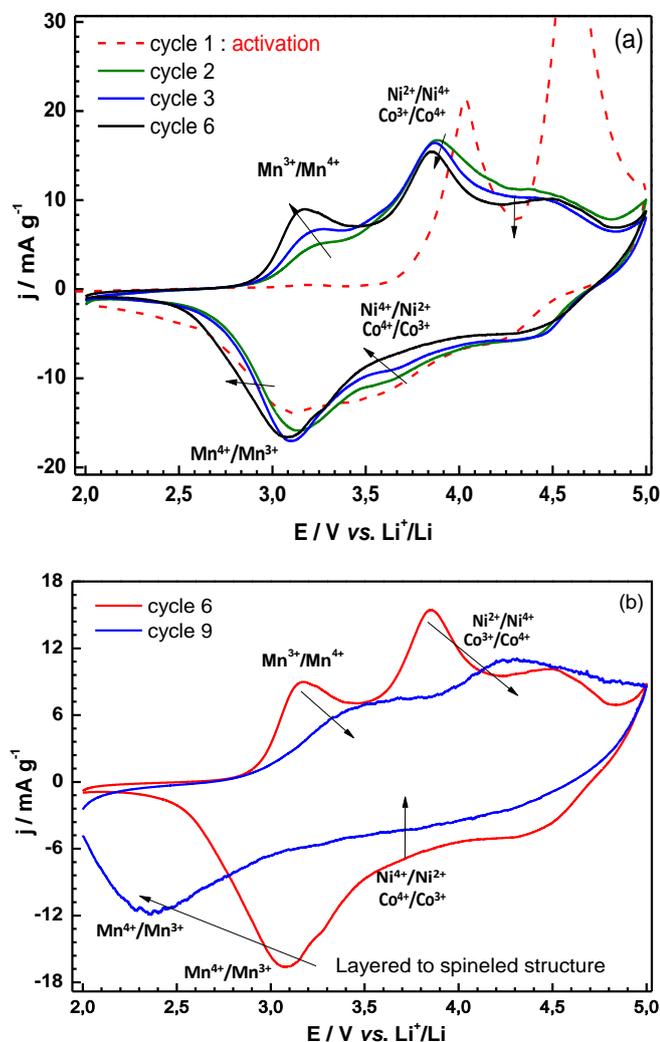

Figure 2. Charge and discharge CV profiles for the first to sixth cycle (a) and sixth to ninth cycles (b) for the Li-rich-NMC cathode in half Swagelok at 20 μV s⁻¹

Figure 3a shows the first charge-discharge profiles of the Li-rich-NMC in EC/DMC without (blue curve) and with 1% PS (red and black curves) in four half-cells at a current density of 16 mA g⁻¹ (0.1 C rate) with different cut-off potentials during charge (4.7 and 5.0 V) and discharge (3 V and 2 V). In the first charge profile, a reproducible wide plateau appeared around the high-potential region (4.4−4.7 V), which was ascribed mainly to the electrochemical activation process of the active material, and whose mechanism is still under debate in the literature. [24-26]. A shoulder followed this plateau between 4.7 and 5 V, which was assigned to the structural changes detected previously by cyclic voltammetry. This transformation consumed almost 50 mAh g⁻¹ of the total charge capacity (324 mAh g⁻¹).

Furthermore, activation cut-off potential influenced the initial discharge capacity measured at 2.0 V. Thus, capacity values of 225 mAh g⁻¹ and 275 mAh g⁻¹ (+ 22%) were provided by the half-cells initially charged at 4.7 V and 5 V, respectively. However, if the discharge was stopped at 3 V (before the plateau relative to Mn⁴⁺/Mn³⁺), although the discharge capacity was also higher for the 5 V-

activated system, the relative increase was lower (10% vs. 22%). This proved undoubtedly that activation at 5 V essentially increased the capacity relying on the manganese couple.

Under the same test conditions, full cells with graphite as the negative electrode showed similar charge discharge profiles (Figure 3b). Although there were no great changes in the charge curves during charging, the shape of the discharge curves changed obviously below 4.7 V, especially with the development of an apparent feature at about 3.0 V.
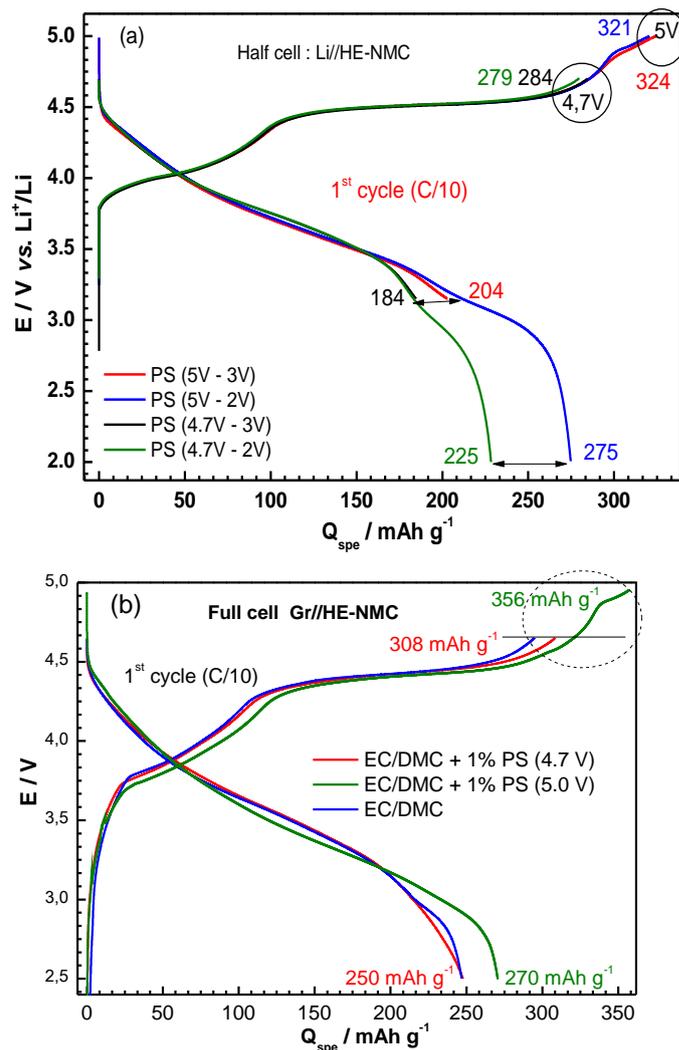

Figure 3. Charge and discharge curves at the first cycle for different cut-off charge potential for half-cell Li//Li-rich-NMC (a), and full-cell Gr//Li-rich-NMC (b) in EC/DMC 1M LiPF₆ + 1% PS at 0.1 C-rate.

Figure 4 shows the temperature effect on the first charge-discharge cycle at the 5 V cut-off potential activation in the presence of 1% PS. The shoulder in the sloping region at 4.8 – 5.0 V, attributed to the structure change (layered to spinel), was more marked at a high temperature. In fact, it consisted of a sloping region and a pseudo-plateau. Meanwhile, on discharge, the high-potential plateau close to 3.7 V shifted abruptly to a new feature at 3.0 V, associated with the spinel structure formed from the layered structure. Therefore, such transformation was accelerated at 60 °C.

It is known that the oxidation voltages as high as 4.7 V lie just above the upper limit of the stability window of alkylcarbonates electrolytes. This leads to deleterious side reactions, which decrease the overall

capacity and cycle life of the cathode [27, 28]. One way to combat this issue is to form a protective film over the active material by coating or by the addition of an additive in the electrolyte. Here, a film formed by a PS additive through its adsorption or a redox reaction could prevent side reactions and dissolution of metal ions.
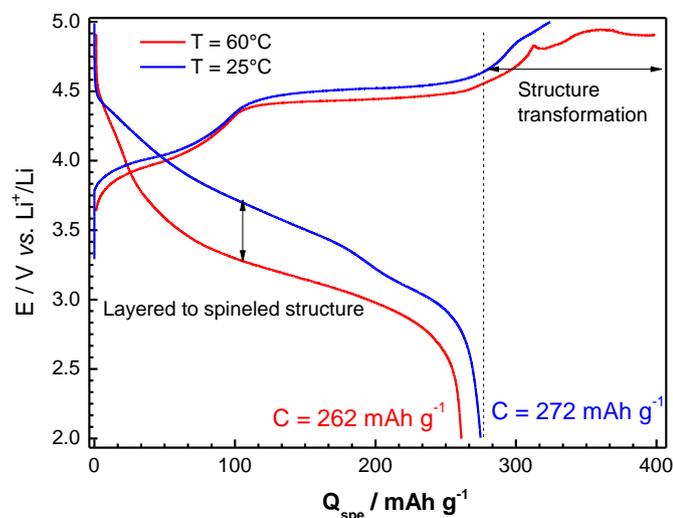
Figure 4 Effect of temperature on charge-discharge curves during the first cycle for half-cell Li//Li-rich-NMC) in EC/DMC 1M LiPF$_6$ + 1% PS at 0.1 C rate.

The above observation suggests that charging at high potential (5 V) should lead to a greater transformation of the layered to spinel structure (as the discharge plateau indicated). While this high potential allows for increased energy, it also exacerbates unwanted side reactions between the active cathode material and the electrolyte solution. Addition of PS can lead to the formation of a protective film at the surface, which in turn can achieve more complete activation.

In this study, competition existed at high potential between structure transformation and manganese dissolution by electrolyte attack and disproportionation of Mn^{3+} as shown in Figure 5.
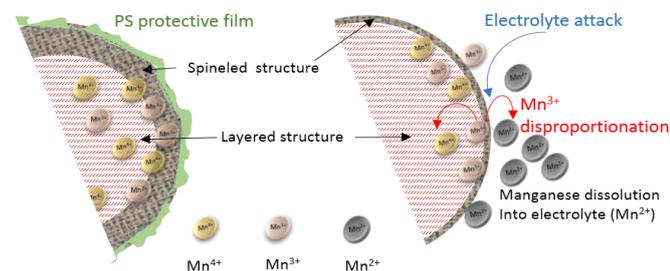

Figure 5 Schematic drawing of the PS protection mechanism on the Li-rich-NMC cathode during cycling and progressive transformation from the layered to the spinel structure.

In the case of a PS-protected interface, the bulk-layered structure to spinel transformation was preserved without the inconvenience of electrode attack by HF or the exposure of Mn^{3+}, prone to disproportion, to the electrolyte. Therefore, manganese dissolution was mitigated and the relative stability of this new spinel during the cycling was high. This was consistent with the maintenance of the manganese plateau observed during the discharge (Figure 5, left), while the non-protected layered structure in the standard electrolyte shrank fast leading to dissolution of transition metal ions (Figure 5, right)[29, 30].

In summary, the addition of PS contributed to the formation of a protective film on the particle surface with the main role of preserving the integrity of the spinel formed at high voltage by protecting the particles from electrolyte erosion and preventing the dissolution of transition metal ions from bulk materials.

3.2.2 Electrochemical impedance spectroscopy characterization

In order to support the above mentioned mechanism, the stability of PS in the high-voltage region was evaluated using EIS as an *in situ* technique to apply a potential signal with 10 mV amplitude in the 20 kHz-2.4 mHz frequency range. Figure 6 shows the Nyquist plots of the electrode charged at 4.6 V, 4.7 V and 5 V vs Li$^+$/Li. For the two first states, where the Li-rich electrode was activated traditionally, the plots could be fitted according to a modified Randles model by the inclusion of two R//C elements). The first element contained an interfacial resistance (R$_{int}$) and capacitance (C$_{int}$), which also observed at OCV (not shown here). However, as grain-grain and grain-collector strains increased on activation, this element developed in the 4.6-4.7 V region. The second R//C element was ascribed to the presence of an adsorbed film formed by electrolyte ions and molecules. Thus, the circuit contained an adsorbed film capacitance (C$_{ads}$) and resistance (R$_{ads}$).
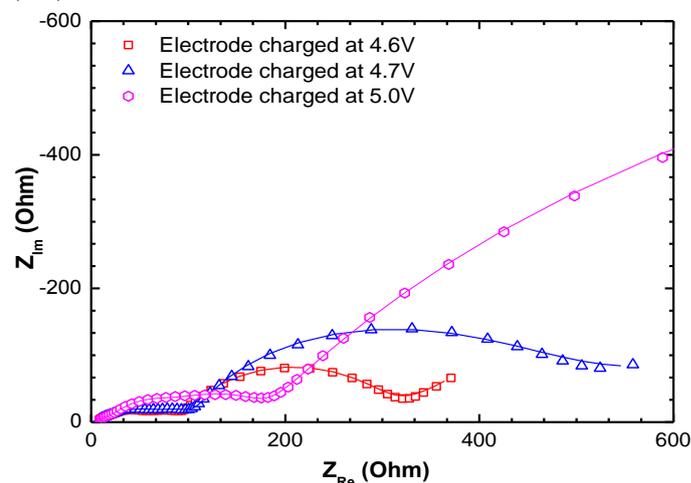

Figure 6. Electrochemical impedance spectroscopy plots of Li-rich-NMC charged at 4.6 V, 4.7 V and 5 V *vs* Li$^+$/Li recorded in the three electrode cells at 25 °C in EC/DMC 1M LiPF$_6$ + 1% PS. Dots and lines correspond to experimental and fitted results.

The presence of an adsorbed film (instead of a solid film) on the electrode surface was consistent with the stability of the electrolyte components up to 4.7 V. Interestingly, the charge transfer resistance (from 205 Ω to 240 Ω) after traditional activation, indicates good electrode/electrolyte interfacial properties for this cathode/electrolyte couple. However, when charged up to 5.0 V, the Nyquist plots could not be fitted with the circuit described above. Instead, a Randles classic circuit containing the R$_{int}$//C$_{int}$ element and the two other R//C elements associated with two solid films can describe the interfacial issues.

Therefore, raising the potential to 5 V displaced the adsorbed film and created two solid interfaces on the electrode. These solid films may be formed by the degradation of PS at such high potential and can consist of sulfur-containing derivatives. Furthermore, independently on these resistive films, a huge increase of the R$_{ct}$ (from 240 Ω to 1300 Ω) was shown, which is consistent with deep reorganization of the system at 5V that worsens the electrode electronic properties. This latter characteristic is in agreement with the mechanism proposed above.

3.2.3 XPS characterization

X-ray Photoelectron Spectroscopy (XPS) was used to further investigate the formation of a protective film at the electrode surface at high-voltage. Figure 7 shows O 1s XPS spectra of the starting electrode (before any cycling) compared to charged electrodes (4.6 V, 4.7 V and 5 V) with electrolyte EC/DMC+ 1% PS + 1M LiPF$_6$. The grey peak around 529.9 eV is attributed to oxygen anions in the active material structure. Peaks at higher binding energies are due to the presence of oxygenated surface species (adsorbed species for the starting electrode). The intensity of material oxygen peak, dominating the O 1s spectrum before cycling, decreases significantly upon the first charge. As the experiment is probing around the first 5 nm of the surface, the less intense the active material peak, the more the surface is covered by deposited oxygenated species. This is in agreement with the presence of a thickening passivation layer up to 5V. Low sulfur contents at the surface (maximum 1% for 5V) compared to the great amounts of oxygenated species deposited in the film suggest that PS acts as a catalyst for reactions involving the solvents and leading to passivation of the surface.
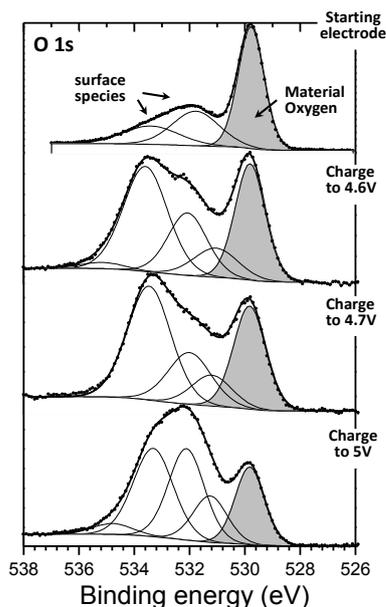

Figure 7. O 1s XPS spectra of positive electrodes before cycling (starting electrode) and charged up to 4.6 V, 4.7 V and 5 V *vs* Li$^+$/Li with EC/DMC + 1% PS + 1M LiPF$_6$.

3.2.4 Cycle-ability characterization

With the purpose of determining the effectiveness of the protection based on PS when cycling with 5 V as the upper voltage limit and maintaining the cycle retention of the Li-rich-NMC cathode, long-cycle tests were carried out at 25 °C in a half-cell configuration. In our tests, the activation was conducted in the first cycle at 0.1 C rate; subsequently, the cell was cycled in the 2.0 V-5.0 V range for 100 cycles at C rate and finally 150 times at 0.2 C rate. The observed decreased capacity on prolonged cycling in the conventional electrolyte as alkylcarbonates was generally associated with both reduction of the oxygen vacancies and lithium sites of the bulk structure and (or) the decomposition reactions of the electrolytes at high operating potential [31, 32]. Figure 8a shows the results obtained with the PS additive. Capacity retention in the presence of 1% PS was 88.4% after 240 cycles (0.2 C). Moreover, the cells exhibited an average value of coulombic efficiency close to 99 %. By comparison,

in the same electrolyte without PS, the decrease in capacity exceeds 50% for 100 cycles (0.2 C).. Figure 8b represents the calculated energy in Wh kg^{-1} of active material for the last 100 cycles (from 140 to 240). Loss in normalized energy was less than 10% in the same cycle range. The midpoint voltages of cathodes, which is an important parameter for high energy density Li-ion batteries, is displayed in inset of Figure 8. At the 200th cycle, the midpoint voltage during discharge for a cathode material cycled in the PS additive based electrolyte was from 3.42 to 3.31 V.
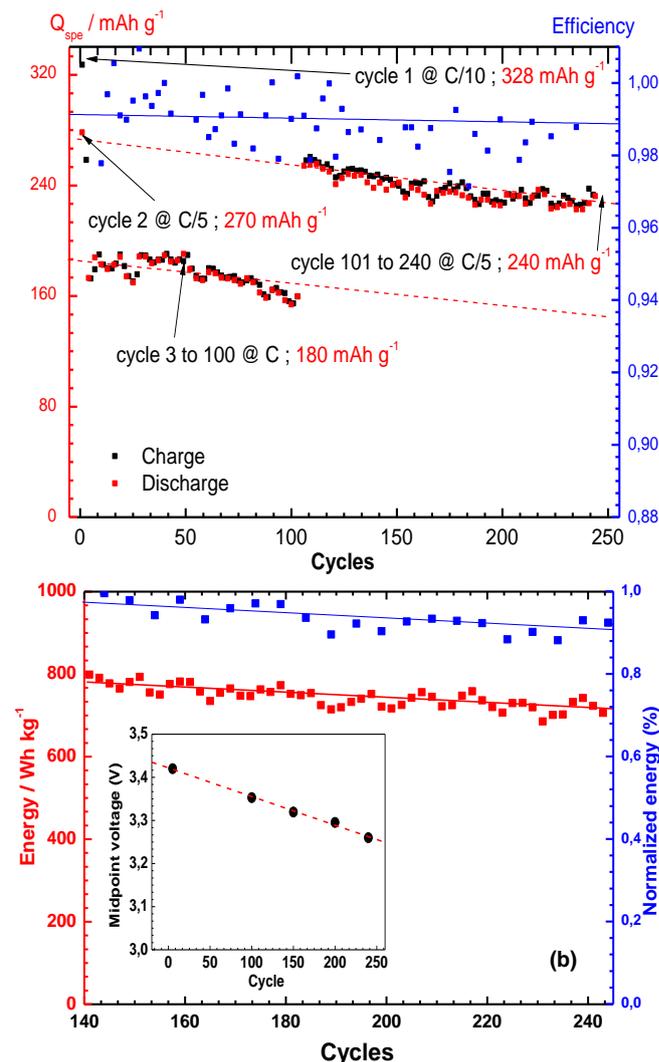
Figure 8. Discharge capacity and efficiency data as function of cycle at different scan rates (a) and Energy (b) of Li-rich-NMC EC/DMC 1M LiPF$_6$ + 1% PS in the 2.0–5.0 V potential range at 25 °C.

Conclusions

Based on the experimental results of this study, a number of conclusions were derived. Firstly, we showed that propane sultone was an efficient additive in EC/DMC 1 M LiPF$_6$ to form a protective film on Li-rich-NMC with a wide electrochemical stability window (5.0 V). It is plausible that a thin layer of PS on Li-rich-NMC particles could provide the necessary protection of the outer surface material from electrolyte attack and prevent side reactions and dissolution of metal ions. Secondly, this protection allowed further activation at a potential higher than the conventional 4.6V proposed for Li-rich-NMC materials. This "new" activation step at 5V probably led to the

transformation of the bulk-layered structure to a spinel phase with substantial manganese rearrangement, resulting accessory manganese redox activity at voltages lower than 3.0 V. Transformation was also strongly affected by temperature and controlled by the initial charge-discharge cut-off voltage. We showed by cyclic voltammetry, galvanostatic measurements and EIS that the continuous increase of the stable manganese in a spinel structure at the surface could protect the cathode from etching by the generated HF in the electrolyte at high potential. This protection suppresses degradation of the cathode and restrains the dissolution of transition metal ions from bulk materials, and thus improves the long-term cycling stability of the cathode but no prevent the midpoint voltages fading.

Notes and references

[a] PCM2E, EA 6299, Université F. Rabelais de Tours, Parc de Grandmont, 37200 Tours, France.*E-mail: meriem.anouti@univ-tours.fr. Tel: (33)247366951.

[b] IPREM, CNRS, University of Pau, Helioparc, 2 av. du Prés. Angot, 64053 Pau cedex 09, France

[c] SAFT, b Saft, 111 Boulevard Alfred Daney, 33074 Bordeaux Cedex, France

[d] UMICORE, Broekstraat 31, 1000 Brussels, Belgium

1. H. Yu and H. Zhou, *The Journal of Physical Chemistry Letters*, 2013, **4**, 1268-1280.
2. F. Cheng, J. Liang, Z. Tao and J. Chen, *Advanced Materials*, 2011, **23**, 1695-1715.
3. H. Yu, H. Kim, Y. Wang, P. He, D. Asakura, Y. Nakamura and H. Zhou, *Physical Chemistry Chemical Physics*, 2012, **14**, 6584-6595.
4. S. Qiu, Z. Chen, F. Pei, F. Wu, Y. Wu, X. Ai, H. Yang and Y. Cao, *European Journal of Inorganic Chemistry*, 2013, **2013**, 2887-2892.
5. X. Yu, Y. Lyu, L. Gu, H. Wu, S.-M. Bak, Y. Zhou, K. Amine, S. N. Ehrlich, H. Li, K.-W. Nam and X.-Q. Yang, *Advanced Energy Materials*, 2014, **4**, n/a-n/a.
6. Y. Gao, J. Ma, X. Wang, X. Lu, Y. Bai, Z. Wang and L. Chen, *Journal of Materials Chemistry A*, 2014, **2**, 4811-4818.
7. S. K. Martha, J. Nanda, Y. Kim, R. R. Unocic, S. Pannala and N. J. Dudney, *Journal of Materials Chemistry A*, 2013, **1**, 5587-5595.
8. X. Yang, D. Wang, R. Yu, Y. Bai, H. Shu, L. Ge, H. Guo, Q. Wei, L. Liu and X. Wang, *Journal of Materials Chemistry A*, 2014, **2**, 3899-3911.
9. A. Boulineau, L. Simonin, J.-F. Colin, C. Bourbon and S. Patoux, *Nano Letters*, 2013, **13**, 3857-3863.
10. L. Zhang, B. Wu, N. Li, D. Mu, C. Zhang and F. Wu, *Journal of Power Sources*, 2013, **240**, 644-652.
11. L. Zhang, W. Borong, L. Ning and W. Feng, *Electrochimica Acta*, 2014, **118**, 67-74.
12. D. Aurbach, K. Gamolsky, B. Markovsky, Y. Gofer, M. Schmidt and U. Heider, *Electrochimica Acta*, 2002, **47**, 1423-1439.
13. M. Lu, H. Cheng and Y. Yang, *Electrochimica Acta*, 2008, **53**, 3539-3546.
14. M. Q. Xu, W. S. Li, X. X. Zuo, J. S. Liu and X. Xu, *Journal of Power Sources*, 2007, **174**, 705-710.
15. J. Li, W. Yao, Y. S. Meng and Y. Yang, *The Journal of Physical Chemistry C*, 2008, **112**, 12550-12556.
16. E. P. Roth, D. H. Doughty and J. Franklin, *Journal of Power Sources*, 2004, **134**, 222-234.
17. S. Tan, Z. Zhang, Y. Li, Y. Li, J. Zheng, Z. Zhou and Y. Yang, *Journal of The Electrochemical Society*, 2013, **160**, A285-A292.
18. S. J. Lee, J.-G. Han, I. Park, J. Song, J. Cho, J.-S. Kim and N.-S. Choi, *Journal of The Electrochemical Society*, 2014, **161**, A2012-A2019.
19. H. Lee, S. Choi, S. Choi, H.-J. Kim, Y. Choi, S. Yoon and J.-J. Cho, *Electrochemistry Communications*, 2007, **9**, 801-806.
20. U. von Sacken, E. Nodwell, A. Sundher and J. R. Dahn, *Journal of Power Sources*, 1995, **54**, 240-245.
21. K.-K. Lee, W.-S. Yoon, K.-B. Kim, K.-Y. Lee and S.-T. Hong, *Journal of The Electrochemical Society*, 2001, **148**, A716-A722.
22. L. El Ouatani, R. Dedryvère, C. Siret, P. Biensan, S. Reynaud, P. Iratçabal and D. Gonbeau, *Journal of The Electrochemical Society*, 2009, **156**, A103-A113.
23. A. R. Armstrong, M. Holzapfel, P. Novák, C. S. Johnson, S.-H. Kang, M. M. Thackeray and P. G. Bruce, *Journal of the American Chemical Society*, 2006, **128**, 8694-8698.
24. M. M. Thackeray, S.-H. Kang, C. S. Johnson, J. T. Vaughey, R. Benedek and S. A. Hackney, *Journal of Materials Chemistry*, 2007, **17**, 3112-3125.
25. S. Hy, F. Felix, J. Rick, W.-N. Su and B. J. Hwang, *Journal of the American Chemical Society*, 2014, **136**, 999-1007.
26. M. Sathiya, A. M. Abakumov, D. Foix, G. Rousse, K. Ramesha, M. Saubanère, M. L. Doublet, H. Vezin, C. P. Laisa, A. S. Prakash, D. Gonbeau, G. VanTendeloo and J. M. Tarascon, *Nat Mater*, 2015, **14**, 230-238.
27. S. A. Freunberger, Y. Chen, Z. Peng, J. M. Griffin, L. J. Hardwick, F. Bardé, P. Novák and P. G. Bruce, *Journal of the American Chemical Society*, 2011, **133**, 8040-8047.
28. G. BrucePeter, A. FreunbergerStefan, J. HardwickLaurence and M. TarasconJean, *Nat Mater*, 2012, **11**, 172-172.
29. D. Tang, L. Ben, Y. Sun, B. Chen, Z. Yang, L. Gu and X. Huang, *Journal of Materials Chemistry A*, 2014, **2**, 14519-14527.
30. A. Manthiram, K. Chemelewski and E.-S. Lee, *Energy & Environmental Science*, 2014, **7**, 1339-1350.
31. P. Oh, S. Myeong, W. Cho, M.-J. Lee, M. Ko, H. Y. Jeong and J. Cho, *Nano Letters*, 2014, **14**, 5965-5972.
32. J. Zhang, J. Wang, J. Yang and Y. NuLi, *Electrochimica Acta*, 2014, **117**, 99-104.